HHS Public Access

Author manuscript

Clin Cancer Res. Author manuscript; available in PMC 2021 March 22.

Published in final edited form as:

Clin Cancer Res. 2018 July 01; 24(13): 3137–3148. doi:10.1158/1078-0432.CCR-17-1957.

Hyperpolarized [1-^{13}C]-Pyruvate Magnetic Resonance Spectroscopic Imaging of Prostate Cancer *In Vivo* Predicts Efficacy of Targeting the Warburg Effect

Bradley T. Scroggins[1], **Masayuki Matsuo**[2], **Ayla O. White**[1], **Keita Saito**[2], **Jeeva P. Munasinghe**[3], **Carole Sourbier**[4], **Kazutoshi Yamamoto**[2], **Vivian Diaz**[3], **Yoichi Takakusagi**[5], **Kazuhiro Ichikawa**[6], **James B. Mitchell**[2], **Murali C. Krishna**[2], **Deborah E. Citrin**[1]

[1]Radiation Oncology Branch, Center for Cancer Research, NCI, NIH, Bethesda, Maryland [2]Radiation Biology Branch, Center for Cancer Research, NCI, NIH, Bethesda, Maryland [3]National Institute of Neurological Disorder and Stroke, NIH, Bethesda, Maryland [4]Urologic Oncology Branch, Center for Cancer Research, NIH, Bethesda, Maryland [5]Department of Molecular Imaging and Theranostics, National Institute of Radiological Sciences, National Institutes for Quantum and Radiological Science and Technology, Chiba, Japan [6]Department of Pharmacy, Faculty of Pharmaceutical Sciences, Nagasaki International University, Nagasaki, Japan

Abstract

Purpose: To evaluate the potential of hyperpolarized [1-^{13}C]-pyruvate magnetic resonance spectroscopic imaging (MRSI) of prostate cancer as a predictive biomarker for targeting the Warburg effect.

Experimental Design: Two human prostate cancer cell lines (DU145 and PC3) were grown as xenografts. The conversion of pyruvate to lactate in xenografts was measured with hyperpolarized [1-^{13}C]-pyruvate MRSI after systemic delivery of [1-^{13}C] pyruvic acid. Steady-state metabolomic analysis of xenograft tumors was performed with mass spectrometry and steady-state lactate concentrations were measured with proton (^{1}H) MRS. Perfusion and oxygenation of xenografts were measured with electron paramagnetic resonance (EPR) imaging with OX063. Tumor growth was assessed after lactate dehydrogenase (LDH) inhibition with FX-11 (42 μg/mouse/day for 5

Corresponding Author: Deborah E. Citrin, NCI, Building 10, Hatfield CRC, B2-3500, Bethesda, MD 20892. Phone: 301-496-5457; Fax: 301-480-5439; citrind@mail.nih.gov.

Authors' Contributions

Conception and design: B.T. Scroggins, M.K. Cherukuri, D.E. Citrin

Development of methodology: B.T. Scroggins, M. Matsuo, K. Ichikawa, J.B. Mitchell, M.K. Cherukuri, D.E. Citrin

Acquisition of data (provided animals, acquired and managed patients, provided facilities, etc.): B.T. Scroggins, M. Matsuo, A.O. White, K. Saito, J.P. Munasinghe, C. Sourbier, K. Yamamoto, V. Diaz, D.E. Citrin

Analysis and interpretation of data (e.g., statistical analysis, biostatistics, computational analysis): Y. Takakusagi, B.T. Scroggins, M. Matsuo, A.O. White, K. Saito, J.P. Munasinghe, C. Sourbier, K. Yamamoto, M.K. Cherukuri, D.E. Citrin

Writing, review, and/or revision of the manuscript: Y. Takakusagi, B.T. Scroggins, A.O. White, K. Yamamoto, J.B. Mitchell, D.E. Citrin

Administrative, technical, or material support (i.e., reporting or organizing data, constructing databases): B.T. Scroggins, M. Matsuo, K. Ichikawa, D.E. Citrin

Study supervision: B.T. Scroggins, M.K. Cherukuri, D.E. Citrin

Disclosure of Potential Conflicts of Interest

No potential conflicts of interest were disclosed.

Note: Supplementary data for this article are available at Clinical Cancer Research Online (http://clincancerres.aacrjournals.org/).

days × 2 weekly cycles). Lactate production, pyruvate uptake, extracellular acidification rates, and oxygen consumption of the prostate cancer cell lines were analyzed *in vitro*. LDH activity was assessed in tumor homogenates.

Results: DU145 tumors demonstrated an enhanced conversion of pyruvate to lactate with hyperpolarized [1-^{13}C]-pyruvate MRSI compared with PC3 and a corresponding greater sensitivity to LDH inhibition. No difference was observed between PC3 and DU145 xenografts in steady-state measures of pyruvate fermentation, oxygenation, or perfusion. The two cell lines exhibited similar sensitivity to FX-11 *in vitro*. LDH activity correlated to FX-11 sensitivity.

Conclusions: Hyperpolarized [1-^{13}C]-pyruvate MRSI of prostate cancer predicts efficacy of targeting the Warburg effect.

Introduction

Prostate cancer accounts for 1 in 5 cancer diagnoses and 8% of cancer deaths in men in the United States (1). Prostate cancer is a heterogeneous disease, with marked variability in aggressiveness and metastatic potential. Androgen deprivation is a common and effective treatment for metastatic prostate cancer; however, metastatic prostate cancer eventually develops resistance to castration with few remaining therapeutic options. The prevalence and inevitable incurability of metastatic prostate cancer supports the need to develop novel therapeutic approaches.

The tendency of cancer cells to ferment glucose to lactate, even in the presence of oxygen, is a hallmark of cancer (2). Increased uptake of glucose, enhanced metabolism of glucose to lactate, and the resulting acidification of the extracellular environment can contribute to tumor cell growth and aggressiveness via a variety of mechanisms, such as enhanced invasiveness and alterations in the tumor immune environment (3, 4). The degree to which glycolysis is preferred is variable among tumor cells (5). Mutations in oncogenes or tumor suppressor genes can have a key role in driving metabolic alterations in tumor cells (6). Characteristics of the tumor microenvironment, such as hypoxia, and exposure to growth factors may also stimulate glucose uptake and glycolysis (7, 8). As multiple variables can affect tumor cell preference for glycolysis, predicting the reliance of specific tumors on glycolysis, and their sensitivity to inhibitors of glycolysis, is challenging.

For the past several decades, noninvasive methods to assess metabolism, such as proton magnetic resonance spectroscopy (^{1}H MRS), have relied on analysis of steady-state levels of important metabolites and intermediates to understand the role of metabolism in tumor progression and in response to therapy (9, 10). More recently, MRS of hyperpolarized compounds has provided the opportunity to evaluate the conversion kinetics of the hyperpolarized substrate to metabolites *in vivo*, effectively allowing real time visualization of the reaction (10). Noninvasive MRSI of hyperpolarized ^{13}C-labeled pyruvate (hyperpolarized ^{13}C-pyruvate MRSI) and its metabolite lactate has been used to image the real time metabolic flux in solid tumors (11) and predicts for tumor response to chemotherapy, radiation, and agents targeting mTOR (12–15).

During hyperpolarized [1-^{13}C]-pyruvate MRSI, a bolus of hyperpolarized ^{13}C-labeled pyruvate is delivered systemically, and its metabolism to lactate is observed in the imaged region. Thus, the flux through enzymatic conversion is interrogated instead of steady-state levels of pyruvate and lactate. Relying on steady-state levels of metabolites may be confounding due to an immediate conversion or utilization of lactate or redistribution through active transport into the circulation or surrounding tissue (16). We hypothesized that the pyruvate fermenting potential, determined by hyperpolarized ^{13}C-pyruvate MRSI, provides a method to predict tumor response to lactate dehydrogenase (LDH) inhibition. In this study, we demonstrate that hyperpolarized ^{13}C-pyruvate MRSI detects metabolic differences in prostate tumor xenografts that are not detectable by steady-state metabolic profiling or steady-state imaging. Further, our data in two prostate cancer xenografts suggest that sensitivity to FX-11, an LDH inhibitor, is predicted with hyperpolarized ^{13}C MRSI in contrast to methods that assess metabolic steady state.

Materials and Methods

Cell culture and transduction

The PC3 and DU145 (prostate carcinoma) cell lines were obtained from the ATCC) and transfected with a lentivirus (LVpFUGW-UbC-ffLuc2-eGFP2, a kind gift of Phillip Tofilon) as described previously (17). Cells were cultured at 37°C in a humidified atmosphere with 5% CO_2 and maintained in RPMI 1640 with 2 mmol/L L-glutamine and HEPES (ATCC) supplemented with 10% fetal bovine serum (Gemini Bio-Products). Cells were authenticated by STR testing (conducted in 2016, performed by ATCC) and used within the first 15 passages. Molecular testing of cell lines for multiple pathogens, including mycoplasma, was performed at the time of receipt and prior to *in vivo* studies.

Animal studies

Animal studies were performed under an institutionally approved protocol in accordance with the guidelines of the Institute of Laboratory Animal Resources, National Research Council. Mice were singly housed and fed a diet of animal chow and water *ad libitum*. PC3 or DU145 tumor cells (1×10^6) were injected subcutaneously into the right hind leg of 9-week-old male athymic nude mice (NCI Frederick). Tumor volumes, calculated by the formula [volume = (width^2 × length)/2], were measured three times weekly.

To assess the effects of LDH inhibition *in vivo*, mice were randomized to treatment groups at a mean tumor volume of 172 mm^3. Immediately after randomization, mice received treatment (intraperitoneal) with vehicle (5% DMSO in DPBS) or FX-11 (42 μg/mouse) for 5 consecutive days, for two weekly cycles. Tumor growth to 1,000 mm^3 was scored for each individual animal. A total of 24 mice were treated per condition and cell line across triplicate experiments.

Hyperpolarized ^{13}C MRSI

For imaging studies, mice were anesthetized with isoflurane (4% induction, 1.5–2.5 maintenance) in medical air (700 mL/minute) and breathing rate was maintained at 80 ± 15 breaths per minute. Core body temperature was maintained at 36 ± 1°C with a flow of warm

air. The lateral tail vein was cannulated with a 30-gauge needle extended with polyethylene tubing (PE-10). Details of hyperpolarization, dissolution, and administration to mice were described earlier (15). A total of 30 μL of [1-^{13}C] pyruvic acid, containing 15 mmol/L OX063 and 2.5 mmol/L gadolinium chelate ProHance (Bracco Diagnostics), was hyperpolarized for 40 to 60 minutes using a Hypersense DNP polarizer (Oxford Instruments). The hyperpolarized [1-^{13}C] pyruvic acid was rapidly dissolved in 4.5 mL of alkaline buffer (50 mmol/L Tris, 60 mmol/L of NaCl, 100 mg/L ethylendiaminetetraacetic acid) and 300 μL of the hyperpolarized [1-^{13}C]-pyruvate solution was injected intravenously. MRI scans were performed on a 4.7 T scanner (Bruker) for baseline studies or a 3 T scanner (MR Solutions) for FX-11 based studies using a 17 mm custom-built ^{13}C solenoid coil placed inside of a saddle coil for ^{1}H. Dynamic ^{13}C-CSI was carried out using the 4.7 T scanner. Images were acquired every 6 up to 240 seconds, with a field of view (FOV) of 32 × 32 mm^2 in an 8 mm axial slice through the tumor, matrix size of 12 × 12, TR of 41.6 ms, and excitation pulse with a flip angle of 10°. For studies completed on the 3T scanner, T2-weighted anatomical images were obtained using a fast spin echo sequence in axial and coronal view with FOV of 28 × 28 or 32 × 32 mm^2, slice thickness of 2 mm, TR of 2,500 or 3,000 ms, and resolution of 0.22 × 0.22 or 0.125 × 0.125 mm. ^{13}C-MRSI was acquired beginning 30 seconds after the start of the pyruvate injection, with a 28 × 28 mm^2 field of view in an 8 mm axial slice through the tumor, a matrix size of 14 × 14, TR of 85 ms, and excitation pulse with a flip angle of 10°. The slab in ^{13}C-MRSI was selected from the anatomical image to minimize inclusion of bone and maximize inclusion of tumor.

^{1}H MRSI

Axial and coronal sets of T_1-weighted axial slices, encompassing the tumor were acquired to delineate anatomical details and specify a voxel (5–7 mm^3) positioned in the tumor that avoided the inclusion on nontumor tissue. An MR spectrum of the dominant water peak within that voxel was acquired using a Point Resolved Spectroscopy (PRESS) pulse sequence (*TR*/*TE* = 2,500/16 ms, *NA* = 1, 2K data points) and was used to optimize so that the magnetic field experienced within the localized voxel was homogenous. The effectiveness of field optimization was measured by evaluating the spectral line width at half height of the water peak (average 23.3 Hz). The PRESS sequence was repeated twice more (at TE = 14 ms and at 140 ms) after incorporating solvent suppressing pulse sequence (VAPOR) to suppress the water peak (NA = 512, total scan time = 25 minutes) and to visualize the metabolite peaks.

The water-suppressed ^{1}H-MR spectra were processed and spectral chemical shifts were assigned with respect to the creatine peak (3.05 ppm). Analysis of the spectra was confined to a selected number of metabolite peaks that corresponded to creatine (3.05 ppm), choline (3.22 ppm), lactate (1.33 ppm), and fat (1.2 ppm) which were evaluated by deconvoluting those peaks to a Lorenzian line shape and calculating the areas under those peaks using XWIN-NMR software (Bruker Biospin Corporation) that were proportional to the metabolite concentrations within the chosen voxel.

Electron paramagnetic resonance (EPR) imaging

Tumor pO_2 maps were obtained using EPR imaging. Technical details were described previously (18, 19). Briefly, anesthetized mice were positioned prone with a tumor-bearing leg placed inside a resonator. A triarylmethyl radical probe OX063 was injected intravenously as a 1.125 mmol/kg bolus through the cannula placed in the tail vein. EPR signals were acquired 3 to15 minutes after the OX063 injection as described earlier (18, 19). Anatomical images were obtained using a 1 T MRI controlled with ParaVision 6.0.1 (Bruker). T_2-weighted anatomical images were obtained using a fast spin echo sequence with TE of 50 ms, TR of 2,000 ms, 14 slices, RARE factor 8, resolution of 0.22 × 0.22 mm, the field of view of 28 mm × 28 mm, and slice thickness of 2 mm. Coregistration of EPR oxygen images and MRI anatomical images was accomplished using a code written in MATLAB (Mathworks) as described in the previous report (18).

Immunoblotting

Treated cells and xenografts were lysed in radioimmunoprecipitation assay buffer (RIPA buffer, Thermo Scientific) supplemented with protease and phosphatase inhibitors (Roche). Protein concentrations were measured by bicinchoninic acid assay (BCA protein assay, Thermo Fisher Scientific), and equal amounts of proteins were separated by SDS-PAGE (Thermo Fisher Scientific). Proteins were transferred to polyvinylidene difluoride membranes (Bio-Rad) and the levels of specific proteins were determined by immunoblotting with primary antibodies against monocarboxylate transporter 1 (MCT1), MCT4, MYC, hexokinase 2 (HK2), lactate dehydrogenase A (LDHA), phosphotyrosine-10 LDHA, LDHB, pyruvate kinase M2 (PKM2; Cell Signaling Technology), hypoxia inducible factor (HIF)-1α (Cayman Chemicals), and Actin (EMD-Millipore).

Proliferation assay

Cell proliferation was measured using a BrdUrd cell proliferation assay according to the manufacturer's protocol (EMD-Millipore). Briefly, PC3 and DU145 cells maintained in log phase growth were plated in 96-well plates and treated with 0.25, 0.5, 1.5, 5, 15, 30, 60, 120, and 240 μmol/L FX-11 for 24 hours. After fixation and denaturation, BrdUrd incorporation was detected with an anti-BrdUrd antibody and goat antimouse secondary antibody conjugated to peroxidase. Peroxidase activity was quantified using 3, 3′, 5, 5′-Tetramethyl[1, 1′-biphenyl]-4, 4′-diamine (TMB). Colorometric change was quantified using absorbance at 450 nm.

Pyruvate uptake assay

Exponentially growing cells (~70% confluent) were washed with DPBS. RPMI 1640 (with 10% FBS) supplemented with 1 μCi of [2-^{14}C]-pyruvic acid was added to cells for the indicated times. Cells were washed three times with ice cold DPBS and lysed in RIPA buffer. Protein concentrations were used to normalize loading of samples. [2-^{14}C]-pyruvic acid uptake was measured using a Wallac 1409 Liquid Scintillation Counter (Perkin Elmer).

Extracellular acidification rate (ECAR) and oxidative consumption rate (OCR) measurements

ECAR and OCR were measured using an XF96 extracellular flux analyzer (Seahorse Bioscience). Cells were plated an XF96 cell culture plate at a density of 20,000/well and incubated overnight. Prior to measurements growth medium was removed and replaced with XF assay medium (DMEM, 25 mmol/L glucose, 4 mmol/L L-glutamine, and 1 mmol/L pyruvate, no bicarbonate and low phosphate). ECAR and OCR measurements were normalized to protein concentrations.

Lactate assay

Exponentially growing cells were washed with DPBS, and cells were incubated in fresh RPMI 1640 (with 10% FBS) for 6 hours at 37°C and 5% CO_2. The manufacture's protocol (Cayman Chemical Company) was followed. Cells were washed with PBS and harvested with 0.5% Trypsin-EDTA (Life Technologies Corp.). The cell pellet and conditioned culture media were deproteinated on ice with 0.25 mol/L metaphosphoric acid (MPA) and neutralized with 24 mmol/L potassium carbonate. L-lactate was measured in conditioned culture media and the cell pellet using lactate dehydrogenase (LDH) and nicotinamide adenine dinucleotide (NAD^+) to oxidize lactate to pyruvate. A standard curve was used to calculate the total L-lactate amount in each sample, and L-lactate levels were normalized to protein concentration.

Metabolome profiling tumor xenografts

Human Metabolome Technologies America performed capillary electrophoresis mass spectrometry analysis (CE-MS, Carcinoscope). Briefly, tumor xenografts were extracted and frozen at −80°C until extraction. Cells were cultured to logarithmic phase (as described above) and washed with a 5% mannitol solution (wash buffer). Metabolites were extracted with ice cold methanol and filtered with 5 kDa molecular weight cutoff spin columns (EMD-Millipore). Filtrates were evaporated and dry metabolites were analyzed by CE-MS as reported previously (20).

Hyperpolarized [1-^{13}C]-pyruvate NMR and LDH activity assay

Detailed in the Supplementary Methods

Statistical analysis

In vitro experiments were conducted in triplicate and repeated in duplicate experiments unless otherwise noted. Comparisons between conditions were performed with ANOVA with Tukey correction for multiple comparisons. A P value less than 0.05 was considered statistically significant.

Results

DU145 xenografts were more glycolytic than PC3 xenografts as measured by hyperpolarized [1-^{13}C]-pyruvate MRSI

In this study, we compared the glycolytic states of PC3 and DU145, two androgen independent human prostate carcinoma cell lines using hyperpolarized [1-^{13}C]-pyruvate MRSI. T_2-weighted MR images and corresponding ^{13}C-MRI images (Fig. 1A) demonstrate that the hyperpolarized pyruvate was rapidly converted to lactate. As evident by comparing spectra, DU145 tumor xenografts more efficiently converted hyperpolarized ^{13}C pyruvate to lactate compared with PC3 tumor xenografts (Fig. 1A; Supplementary Fig. S1). The ratio of the AUC for lactate versus pyruvate correlates with the rate constant of the reaction from pyruvate to lactate and is a suitable method for quantitation and comparison (21). Thus, the ratio of the [1-^{13}C] lactate AUC to the [1-^{13}C]-pyruvate AUC was calculated from the time intensity curve and compared between DU145 xenografts ($n = 5$) and PC3 xenografts ($n = 5$). As shown in Fig. 1B, the lactate AUC/pyruvate AUC ratio in DU145 tumors was significantly greater than that measured in PC3 xenografts (0.78 vs. 0.57, $P < 0.05$).

Steady-state analysis of lactate and pyruvate in DU145 and PC3 xenografts differs from hyperpolarized [1-^{13}C]-pyruvate MRSI

The conversion of pyruvate to lactate as measured by hyperpolarized [1-^{13}C]-pyruvate MRSI involves the delivery of a pyruvate bolus. To examine the possibility that steady-state ratios of lactate and pyruvate may be different from that observed in the context of hyperpolarized [1-^{13}C]-pyruvate MRSI, and to evaluate the overall glycolytic potential of DU145 and PC3 xenografts, we performed quantitative metabolome profiling. The relative levels of metabolites in DU145 and PC3 xenograft tumors ($n = 3$ per cell line) were compared with specific interest in metabolites involved in glycolysis. As noted in Table 1, levels of lactic acid and pyruvic acid were not statistically different between DU145 and PC3 tumors; however, the ratio of lactic acid to pyruvic acid was significantly higher in PC3 tumors (173 ± 21 vs. 97 ± 27, $P = 0.021$). Interestingly, quantitative metabolome profiling demonstrated a higher ratio of lactate/pyruvate in PC3 tumors, in contrast to the higher lactate/pyruvate ratio seen in DU145 with hyperpolarized [1-^{13}C]-pyruvate MRSI.

In metabolome profiling, PC3 demonstrated minimally increased lactate compared with pyruvate ($P = 0.403$). For further confirmation that steady-state lactate was not higher in DU145 compared with PC3, as would be predicted based on hyperpolarized [1-^{13}C]-pyruvate MRSI, steady-state lactate and creatine in DU145 and PC3 xenografts was measured with ^{1}H-MRSI. The mean lactate/creatine ratio in PC3 tumors ($n = 5$) as assessed with ^{1}H-MRSI was 1.7-fold higher than that observed in DU145 tumors ($P = 0.21$; Fig. 1C). Using levels obtained with metabolome profiling, a similar pattern in the lactic acid/creatine ratio was observed when comparing PC3 and DU145 (ratio 1.8, $P = 0.203$). Collectively, these data demonstrate that pyruvate metabolism to lactate as extrapolated from steady-state assessment of pyruvate and lactate ratios and pyruvate and creatine ratios do not agree with the findings of hyperpolarized [1-^{13}C]-pyruvate MRSI.

DU145 xenografts demonstrate growth inhibition after FX-11 treatment and reduced conversion of [1-^{13}C] pyruvate to [1-^{13}C] lactate

Hyperpolarized [1-^{13}C]-pyruvate MRSI suggested enhanced conversion of pyruvate to lactate in DU145 tumors compared with PC3 tumors. Based on these findings, we hypothesized that DU145 xenografts would preferentially exhibit a growth delay after LDH-A inhibition compared with PC3 xenografts. Mice bearing DU145 and PC3 xenografts were randomized and treated daily for 5 consecutive days per week for 2 weeks with FX-11 or vehicle. PC3 tumor growth was not affected by LDH-A inhibition with FX-11, whereas the growth of DU145 tumors was significantly reduced by FX-11 treatment (Fig. 2).

To determine the utility of hyperpolarized [1-^{13}C]-pyruvate conversion to lactate as a biomarker for sensitivity to LDH-A inhibition, mice bearing PC3 and DU145 xenografts were evaluated by hyperpolarized MRS before and after FX-11 treatment (FX-11, 42 μg/mouse per day for 2 days, imaging 1 hour after second dose). As shown in Fig. 3, PC3 tumors exhibited minimal change in lactate/pyruvate ratios when comparing spectra obtained prior to and following FX-11 treatment. In contrast, DU145 tumors demonstrated a significant reduction in pyruvate conversion to lactate after FX-11 treatment. Thus, baseline hyperpolarized [1-^{13}C]-pyruvate MRS accurately predicted response to FX-11 treatment. Further, a preferential capacity of FX-11 to inhibit pyruvate fermentation in DU145 tumors was detectable with hyperpolarized [1-^{13}C]-pyruvate MRSI.

DU145 and PC3 tumors demonstrate similar perfusion and oxygenation

Tumor hypoxia is known to enhance glycolysis, resulting in increased production of lactate. Further, hypoxia enhances LDH-A expression, thus increasing the capacity to reduce pyruvate to lactate (22–24). Evaluation of perfusion and pO_2 in DU145 and PC3 xenograft tumors revealed no significant difference in either measure at baseline and after FX-11 (Fig. 4A–C).

The expression of several proteins involved in pyruvate and lactate metabolism and transport was assessed by Western blotting (Fig. 4D; Supplementary Fig. S1). The expression of HIF-1α was higher in PC3, whereas DU145 xenografts demonstrated higher expression of the LDH-B isoform. MCT4 expression is often upregulated in response to hypoxia and in tumor cells that rely predominantly on glycolysis for energy. The expression of the pyruvate transporter MCT1 was not significantly different, whereas MCT4 expression was higher in DU145 tumors. MCT1 is responsible for pyruvate and lactate uptake, and MCT4 is responsible for lactate extrusion. LDH activity in tumor homogenates was higher for DU145 compared with PC3 (53.95 vs. 34.62 nmol/minute/mg tumor, $P < 0.03$; Supplementary Fig. S5A). Thus, both LDH activity and [1-^{13}C]-pyruvate MRSI predicted tumor response to FX-11.

In vitro assessment of response to LDH-A inhibition

To further evaluate cellular dependence on LDH-A activity, the proliferation of DU145 and PC3 cells was evaluated with varying concentrations of FX-11. The half maximal inhibitory concentration (IC_{50}) for proliferation of DU145 and PC3 cell lines *in vitro* was strikingly similar (32 ± 1.1 μmol/L vs. 27 ± 1.1 μmol/L, respectively, Fig. 5A). Further interrogation of

the metabolic phenotype of the two cell lines *in vitro* demonstrated no significant difference in extracellular acidification rate (ECAR), oxygen consumption rate (OCR), pyruvate uptake, and lactate production (Fig. 5B–E). Expression of MCT1, MCT4, HK2, and LDH-A was similar to that observed *in vivo* (Figs. 4D and 5F). To determine the functional consequences of LDH-A inhibition of the two cancer cell lines to LDH-A inhibition *in vitro*, ECAR was assessed in DU145 and PC3 cells exposed to FX-11 at varying concentrations. The PC3 and DU145 cell lines demonstrated similar sensitivity to ECAR reduction *in vitro* with FX-11 treatment, with an IC_{50} of 23.5 μmol/L for PC3 and 39.9 for DU145 μmol/L ($P = 0.120$).

To explore the possibility that delivery of pyruvic acid to tumor-bearing mice during hyperpolarized [1-^{13}C]-pyruvate MRSI could provide excess substrate for LDH-A and drive the effects observed *in vivo*, ECAR and OCR were analyzed *in vitro* in the presence of excess pyruvate (Fig. 5H and I). Treatment with pyruvate resulted in an immediate reduction in ECAR and increase in OCR in both DU145 and PC3 tumor cells. The effects of pyruvate on ECAR and OCR were more profound in DU145 compared with PC3.

To assess if a differential conversion of hyperpolarized [1-^{13}C] pyruvate to lactate could be observed *in vitro*, hyperpolarized [1-^{13}C]-pyruvate NMR was performed in DU145 and PC3 cells grown in monolayer. The effects of FX-11 in cells grown in tissue culture was analyzed with hyperpolarized [1-^{13}C]-pyruvate NMR (Supplementary Fig. S6). A significant reduction in lactate production with FX-11 treatment was observed in DU145 cells with no significant change in PC3 cells (Supplementary Fig. S6). Collectively, these data support that hyperpolarized [1-^{13}C]-pyruvate MRSI functions as a noninvasive biomarker of metabolic phenotype and response to FX-11.

Discussion

Preferential dependence on glycolysis and production of lactate is a hallmark of cancer (25). Because pyruvate is an end product of glycolysis, the rate of pyruvate production and metabolism may be a marker for glycolytic dependence. A glycolytic phenotype is observed in human prostate cancer tissues with the highest expression of MCT's and glycolytic enzymes in metastatic tissue compared with tumors growing in the prostate (26). Further, elevated expression of glycolytic markers correlates with inferior prognosis after surgery for localized prostate cancer (26). The correlation of prostate cancer aggressiveness and stage with increased expression of glycolytic markers provides a strong rationale for the study of metabolic inhibitors in prostate cancer.

With the growing interest in cancer cell metabolism, the development of agents targeting metabolic adaptations observed in tumors has expanded. DNA mutations and copy-number alterations in diverse genes may alter the metabolic phenotype and reliance on specific metabolic pathways, including mutations in MYC, AKT1, TP53, and PTEN (27–29). Similarly, physiologic aspects of the *in vivo* environment, such as hypoxia, have been demonstrated to affect metabolic dependence on glycolysis. In addition to these complexities, therapeutic interventions, such as androgen deprivation, may also alter the metabolic landscape of prostate cancers (30, 31). Thus, the capacity to integrate this

complexity into a model that predicts an individual tumor's response to metabolic inhibitors remains elusive. The identification of biomarkers capable of predicting efficacy of metabolic inhibitors is needed.

Hyperpolarized [1-^{13}C]-pyruvate MRSI offers a noninvasive approach to interrogate the flux to lactate catalyzed by LDH *in vivo* and thus provides a real-time assessment of metabolism. Studies in murine models and in prostate cancer patients have begun to explore hyperpolarized [1-^{13}C]-pyruvate MRSI as a noninvasive biomarker for prostate cancer detection and grading (10, 32–35) and have demonstrated a strong correlation of pyruvate conversion to lactate in high-grade compared with low-grade tumors. Few studies have evaluated hyperpolarized imaging as a predictive biomarker (36).

In this study, a greater capacity for lactate production was observed in DU145 xenografts compared with PC3 xenografts using hyperpolarized [1-^{13}C]-pyruvate MRSI. The enhanced flux of pyruvate to lactate in DU145 compared with PC3 tumors was not predicted by steady-state metabolome profiling and steady-state imaging of lactate with ^{1}H MRS. This suggests that LDH activity may not be adequately assessed with steady-state assessments.

The discrepancy between lactate:creatine and lactate: pyruvate ratios at steady state compared with hyperpolarized [1-^{13}C]-pyruvate MRSI may be explained by several potential mechanisms which are the focus of ongoing work. It is possible that pyruvate or lactate are used in the *in vivo* setting as a substrate for alternative biochemical reactions and are no longer detected after this consumption using steady-state imaging (37). Alternatively, lactate may be transported outside of the cell after production by MCTs and rapidly dispersed in the blood pool beyond the imaged tumor. It also remains possible that the delivery of a supraphysiologic bolus of pyruvate to tumor may interrogate the capacity of the tumor to catalyze the reaction instead of the basal flux. Previously published data show that a pyruvate bolus may induce hypoxia or alter the metabolism of the tumor *in vivo* hours after a pyruvate bolus is delivered (38, 39), supporting the notion that the kinetics of the reaction are enhanced *in vivo* by the presence of additional substrate. Additionally, hyperpolarized [1-^{13}C]-pyruvate MRSI evaluates the conversion of pyruvate to lactate over minutes and may not provide information about how the kinetics change over time.

In vitro, the DU145 and PC3 prostate cancer cell lines demonstrated a similar metabolic phenotype. These data agree with prior studies that report little difference in lactate production between PC3 and DU145 cell lines grown *in vitro* (26, 40). Further, these findings support the possibility that the preferential conversion of pyruvate to lactate in xenografts is related to a physiologic difference between the *in vitro* and *in vivo* environment, a theory that is supported by the similar sensitivity to FX-11 treatment *in vitro* versus the enhanced sensitivity to DU145 to FX-11 treatment *in vivo*. Hypoxia *in vivo* could explain a preferential dependence on lactic acid fermentation; however, both DU145 and PC3 tumors demonstrated a similar pattern and extent of hypoxia and perfusion as assessed by EPR imaging. The technique used to evaluate hypoxia and perfusion is a point in time assessment and cannot evaluate these dynamic processes over time. Using the EPR method to assess hypoxia and perfusion in tumors of similar size, it can be suggested that delivery of pyruvate (perfusion) and hypoxia did not drive the differential hyperpolarized [1-^{13}C]-

pyruvate MRSI response and FX-11 sensitivity *in vivo*. The discordance of steady-state lactate assessments to hyperpolarized [1-^{13}C]-pyruvate MRSI response, coupled with the differences observed of *in vitro* and *in vivo* tumor cell sensitivity to FX-11, strongly suggest that tumor cell dependence on LDH activity varies substantially between *in vitro* and *in vivo* conditions. We hypothesize that the stromal compartment of these tumors is contributing to this discordance as has been suggested as a possible mechanism of altered lactate utilization *in vivo* (16, 41). In addition, the impact of tumor microenvironment on hyperpolarized [1-^{13}C]-pyruvate MRSI characteristics and as a possible explanation for the discordance of the *in vitro* studies *in vivo* studies presented here cannot be discounted. Prior studies have suggested that tumor cells may develop a symbiotic relationship with surrounding stroma, wherein tumor secretes lactate via MCT4, which is then taken up by stromal cells via MCT1, and utilized as a substrate for oxidative phosphorylation (16, 42). Further, a symbiotic relationship of tumor and stroma can result in transport of lactate from regions of excess to regions low lactate production, where it may serve as a substrate for catabolism (41). These interactions are not possible to interrogate *in vivo* with current techniques, a necessity to clarify if tumor-stroma interactions drive the phenomenon of discordant comparisons between steady-state measures and hyperpolarized [1-^{13}C]-pyruvate MRSI. It is important to note that regardless of the cause of this discrepancy, differential baseline hyperpolarized [1-^{13}C]-pyruvate MRSI response and change in pyruvate conversion to lactate after FX-11 treatment assessed with this imaging modality correlated with LDH activity and sensitivity of the tumors to FX-11.

Importantly, the response of these two prostate cancer cell lines to LDH inhibition would not be expected based on mutational profile and expression of a range of glycolytic markers. A study of pancreatic patient derived xenografts has suggested that p53 status determines sensitivity to LDH-A inhibition with p53 wild-type tumors exhibiting resistance and p53-mutant tumors demonstrating sensitivity (43). Both DU145 and PC3 are p53-mutant lines (44, 45). In contrast to the aforementioned report, we observed that the p53-mutant cell line PC3 had no observable growth delay *in vivo* with LDH-A inhibition, a finding that correlated to a lack of observed change in pyruvate conversion to lactate with hyperpolarized [1-^{13}C]-pyruvate MRSI. Further, we noted no significant difference in the expression of TIGAR, a negative regular of glycolysis whose expression correlated with reduced sensitivity to FX-11 (43, 46).

Similarly, the expression of HK2 driven by loss of PTEN and p53 in prostate cancer cells has been shown to drive the Warburg effect (28). As expected, HK2 expression was increased in the p53-deficient/PTEN-deficient PC3 cells compared with DU145 cells (p53-deficient/PTEN expressing); however, the increased expression of HK2 in PC3 cells did not translate into enhanced dependence of lactic acid fermentation. Similarly, we observed higher expression of LDH-B in DU145 cells compared with PC3 cells and a reverse trend for the expression for LDH-A; however, FX-11 is selective for the LDH-A isoform relative to LDH-B (47, 48). Based on the expression pattern of LDH-A, LDH-B, MCT1, HK2, and other glycolytic enzymes, PC3 would be predicted to more efficiently convert pyruvate to lactate and to have enhanced sensitivity to FX-11 compared with DU145. One could speculate that the higher expression of MCT-4 in DU145 xenografts results in increased pyruvate reduction due to transport of lactate outside of the tumor cell, as previously

reported (49). Further, enhanced LDH-B expression could increase LDH activity if sufficient substrate is present.

The reduction of pyruvate to lactate by LDH is paired with oxidation of nicotinamide adenine dinucleotide (NADH) to NAD^+. Feedback loops function to maintain optimal concentrations of NADH/NAD^+ (50). Increased concentrations of NADH, such as that associated with hypoxia, result in enhanced oxidation of NADH and conversion of pyruvic acid to lactic acid (50). Thus, higher concentrations of NADH or an elevated ratio of NADH/NAD^+ would be anticipated to drive the conversion of pyruvate to lactate. DU145 tumors demonstrated a higher NAD^+ concentration and similar NADH concentrations when compared with PC3, suggesting that NADH/NAD^+ balance is not driving the differences in hyperpolarized [1-^{13}C]-pyruvate MRSI response and FX-11 sensitivity *in vivo.*

Data from the current study are limited to two cell lines with well-described mutational profiles and are derived from metastatic sites, and thus, may be expected to have enhanced glycolytic states. It will be important to expand these findings to additional prostate cancer models such as patient-derived xenografts and patients enrolled on clinical trials.

Collectively, these data suggest that hyperpolarized [1-^{13}C]-pyruvate MRSI is a noninvasive biomarker for efficacy of LDH inhibition. These findings provide a rationale for evaluating hyperpolarized MRS imaging as a predictive biomarker via the interrogation of the flux through specific reactions targeted by metabolic inhibitors.

Supplementary Material

Refer to Web version on PubMed Central for supplementary material.

Acknowledgments

(B. Scroggins, M. Matsuo, A.O. White, K. Saito, C. Sourbier, K. Yamamoto, D. Citrin, M. Krishna, and J.B. Mitchell): This research was supported in part by the Intramural Research Program of the NIH, NCI (ZIA BC 010850, ZIA BC 011552).

(Y. Takakusagi and K. Ichikawa): This work was supported in part by CREST (JPMJCR13L4) and JSPS KAKENHI Grant Number 17K01363 (Y. Takakusagi), 26560215 (K. Ichikawa).

References

1. Siegel RL, Miller KD, Jemal A. Cancer statistics, 2017. CA Cancer J Clin 2017;67:7–30. [PubMed: 28055103]
2. Warburg O On the origin of cancer cells. Science 1956;123:309–14. [PubMed: 13298683]
3. Estrella V, Chen T, Lloyd M, Wojtkowiak J, Cornnell HH, Ibrahim-Hashim A, et al. Acidity generated by the tumor microenvironment drives local invasion. Cancer Res 2013;73:1524–35. [PubMed: 23288510]
4. Chang CH, Qiu J, O'Sullivan D, Buck MD, Noguchi T, Curtis JD, et al. Metabolic competition in the tumor microenvironment is a driver of cancer progression. Cell 2015;162:1229–41. [PubMed: 26321679]
5. Zheng JEnergy metabolism of cancer: Glycolysis versus oxidative phosphorylation (Review). Oncol Lett 2012;4:1151–7. [PubMed: 23226794]
6. Levine AJ, Puzio-Kuter AM. The control of the metabolic switch in cancers by oncogenes and tumor suppressor genes. Science 2010;330: 1340–4. [PubMed: 21127244]

7. Boerner P, Resnick RJ, Racker E. Stimulation of glycolysis and amino acid uptake in NRK-49F cells by transforming growth factor beta and epidermal growth factor. Proc Natl Acad Sci U S A 1985;82:1350–3. [PubMed: 3871948]

8. Hiraki Y, Rosen OM, Birnbaum MJ. Growth factors rapidly induce expression of the glucose transporter gene. J Biol Chem 1988;263: 13655–62. [PubMed: 3262104]

9. Day SE, Kettunen MI, Gallagher FA, Hu DE, Lerche M, Wolber J, et al. Detecting tumor response to treatment using hyperpolarized 13C magnetic resonance imaging and spectroscopy. Nat Med 2007;13: 1382–7. [PubMed: 17965722]

10. Albers MJ, Bok R, Chen AP, Cunningham CH, Zierhut ML, Zhang VY, et al. Hyperpolarized 13C lactate, pyruvate, and alanine: noninvasive biomarkers for prostate cancer detection and grading. Cancer Res 2008;68: 8607–15. [PubMed: 18922937]

11. Dutta P, Le A, Vander Jagt DL, Tsukamoto T, Martinez GV, Dang CV, et al. Evaluation of LDH-A and glutaminase inhibition in vivo by hyperpolarized 13C-pyruvate magnetic resonance spectroscopy of tumors. Cancer Res 2013;73:4190–5. [PubMed: 23722553]

12. Park I, Bok R, Ozawa T, Phillips JJ, James CD, Vigneron DB, et al. Detection of early response to temozolomide treatment in brain tumors using hyperpolarized 13C MR metabolic imaging. J Magn Reson Imaging 2011;33:1284–90. [PubMed: 21590996]

13. Venkatesh HS, Chaumeil MM, Ward CS, Haas-Kogan DA, James CD, Ronen SM. Reduced phosphocholine and hyperpolarized lactate provide magnetic resonance biomarkers of PI3K/Akt/mTOR inhibition in glioblastoma. Neuro Oncol 2012;14:315–25. [PubMed: 22156546]

14. Ward CS, Venkatesh HS, Chaumeil MM, Brandes AH, Vancriekinge M, Dafni H, et al. Noninvasive detection of target modulation following phosphatidylinositol 3-kinase inhibition using hyperpolarized 13C magnetic resonance spectroscopy. Cancer Res 2010;70: 1296–305. [PubMed: 20145128]

15. Saito K, Matsumoto S, Takakusagi Y, Matsuo M, Morris HD, Lizak MJ, et al. 13C-MR spectroscopic imaging with hyperpolarized [1–13C]pyruvate detects early response to radiotherapy in SCC tumors and HT-29 tumors. Clin Cancer Res 2015;21:5073–81. [PubMed: 25673698]

16. Sonveaux P, Vegran F, Schroeder T, Wergin MC, Verrax J, Rabbani ZN, et al. Targeting lactate-fueled respiration selectively kills hypoxic tumor cells in mice. J Clin Invest 2008;118:3930–42. [PubMed: 19033663]

17. Jamal M, Rath BH, Tsang PS, Camphausen K, Tofilon PJ. The brain microenvironment preferentially enhances the radioresistance of CD133 (+) glioblastoma stem-like cells. Neoplasia 2012;14:150–8. [PubMed: 22431923]

18. Matsumoto K, Subramanian S, Devasahayam N, Aravalluvan T, Murugesan R, Cook JA, et al. Electron paramagnetic resonance imaging of tumor hypoxia: enhanced spatial and temporal resolution for in vivo pO2 determination. Magn Reson Med 2006;55:1157–63. [PubMed: 16596636]

19. Matsumoto S, Hyodo F, Subramanian S, Devasahayam N, Munasinghe J, Hyodo E, et al. Low-field paramagnetic resonance imaging of tumor oxygenation and glycolytic activity in mice. J Clin Invest 2008;118: 1965–73. [PubMed: 18431513]

20. Hirayama A, Kami K, Sugimoto M, Sugawara M, Toki N, Onozuka H, et al. Quantitative metabolome profiling of colon and stomach cancer microenvironment by capillary electrophoresis time-of-flight mass spectrometry. Cancer Res 2009;69:4918–25. [PubMed: 19458066]

21. Hill DK, Orton MR, Mariotti E, Boult JK, Panek R, Jafar M, et al. Model free approach to kinetic analysis of real-time hyperpolarized 13C magnetic resonance spectroscopy data. PLoS One 2013;8:e71996. [PubMed: 24023724]

22. Cahn RD, Zwilling E, Kaplan NO, Levine L. Nature and Development of Lactic Dehydrogenases: The two major types of this enzyme form molecular hybrids which change in makeup during development. Science 1962;136:962–9. [PubMed: 17796806]

23. Bishop MJ, Everse J, Kaplan NO. Identification of lactate dehydrogenase isoenzymes by rapid kinetics. Proc Natl Acad Sci U S A 1972; 69:1761–5. [PubMed: 4340158]

24. Semenza GL, Jiang BH, Leung SW, Passantino R, Concordet JP, Maire P, et al. Hypoxia response elements in the aldolase A, enolase 1, and lactate dehydrogenase A gene promoters contain

essential binding sites for hypoxia-inducible factor 1. J Biol Chem 1996;271: 32529–37. [PubMed: 8955077]

25. Hanahan D, Weinberg RA. Hallmarks of cancer: the next generation. Cell 2011;144:646–74. [PubMed: 21376230]
26. Pertega-Gomes N, Felisbino S, Massie CE, Vizcaino JR, Coelho R, Sandi C, et al. A glycolytic phenotype is associated with prostate cancer progression and aggressiveness: a role for monocarboxylate transporters as metabolic targets for therapy. J Pathol 2015;236:517–30. [PubMed: 25875424]
27. Priolo C, Pyne S, Rose J, Regan ER, Zadra G, Photopoulos C, et al. AKT1 and MYC induce distinctive metabolic fingerprints in human prostate cancer. Cancer Res 2014;74:7198–204. [PubMed: 25322691]
28. Wang L, Xiong H, Wu F, Zhang Y, Wang J, Zhao L, et al. Hexokinase 2-mediated Warburg effect is required for PTEN- and p53-deficiency-driven prostate cancer growth. Cell Rep 2014;8:1461–74. [PubMed: 25176644]
29. Graham NA, Minasyan A, Lomova A, Cass A, Balanis NG, Friedman M, et al. Recurrent patterns of DNA copy number alterations in tumors reflect metabolic selection pressures. Mol Syst Biol 2017;13:914. [PubMed: 28202506]
30. Martin PL, Yin JJ, Seng V, Casey O, Corey E, Morrissey C, et al. Androgen deprivation leads to increased carbohydrate metabolism and hexokinase 2-mediated survival in Pten/Tp53-deficient prostate cancer. Oncogene 2017;36:525–33. [PubMed: 27375016]
31. Shafi AA, Putluri V, Arnold JM, Tsouko E, Maity S, Roberts JM, et al. Differential regulation of metabolic pathways by androgen receptor (AR) and its constitutively active splice variant, AR-V7, in prostate cancer cells. Oncotarget 2015;6:31997–2012. [PubMed: 26378018]
32. Lupo JM, Chen AP, Zierhut ML, Bok RA, Cunningham CH, Kurhanewicz J, et al. Analysis of hyperpolarized dynamic 13C lactate imaging in a transgenic mouse model of prostate cancer. Magn Reson Imaging 2010;28: 153–62. [PubMed: 19695815]
33. Wilson DM, Kurhanewicz J. Hyperpolarized 13C MR for molecular imaging of prostate cancer. J Nucl Med 2014;55:1567–72. [PubMed: 25168625]
34. Chen HY, Larson PEZ, Bok RA, von Morze C, Sriram R, Delos Santos R, et al. Assessing prostate cancer aggressiveness with hyperpolarized dual-agent 3D dynamic imaging of metabolism and perfusion. Cancer Res 2017;77: 3207–16. [PubMed: 28428273]
35. Chen AP, Albers MJ, Cunningham CH, Kohler SJ, Yen YF, Hurd RE, et al. Hyperpolarized C-13 spectroscopic imaging of the TRAMP mouse at 3T-initial experience. Magn Reson Med 2007;58:1099–106. [PubMed: 17969006]
36. Keshari KR, Wilson DM, Van Criekinge M, Sriram R, Koelsch BL, Wang ZJ, et al. Metabolic response of prostate cancer to nicotinamide phophoribosyltransferase inhibition in a hyperpolarized MR/PET compatible bioreactor. Prostate 2015;75:1601–9. [PubMed: 26177608]
37. Kennedy KM, Dewhirst MW. Tumor metabolism of lactate: the influence and therapeutic potential for MCT and CD147 regulation. Future Oncol 2010;6:127–48. [PubMed: 20021214]
38. Takakusagi Y, Matsumoto S, Saito K, Matsuo M, Kishimoto S, Wojtkowiak JW, et al. Pyruvate induces transient tumor hypoxia by enhancing mitochondrial oxygen consumption and potentiates the anti-tumor effect of a hypoxia-activated prodrug TH-302. PLoS One 2014;9: e107995. [PubMed: 25254649]
39. Saito K, Matsumoto S, Devasahayam N, Subramanian S, Munasinghe JP, Morris HD, et al. Transient decrease in tumor oxygenation after intravenous administration of pyruvate. Magn Reson Med 2012;67:801–7. [PubMed: 22006570]
40. Higgins LH, Withers HG, Garbens A, Love HD, Magnoni L, Hayward SW, et al. Hypoxia and the metabolic phenotype of prostate cancer cells. Biochim Biophys Acta 2009;1787:1433–43. [PubMed: 19524545]
41. Kennedy KM, Scarbrough PM, Ribeiro A, Richardson R, Yuan H, Sonveaux P, et al. Catabolism of exogenous lactate reveals it as a legitimate metabolic substrate in breast cancer. PLoS One 2013;8:e75154. [PubMed: 24069390]

42. Patel BB, Ackerstaff E, Serganova IS, Kerrigan JE, Blasberg RG, Koutcher JA, et al. Tumor stroma interaction is mediated by monocarboxylate metabolism. Exp Cell Res 2017;352:20–33. [PubMed: 28132882]
43. Rajeshkumar NV, Dutta P, Yabuuchi S, de Wilde RF, Martinez GV, Le A, et al. Therapeutic targeting of the warburg effect in pancreatic cancer relies on an absence of p53 function. Cancer Res 2015;75:3355–64. [PubMed: 26113084]
44. Bajgelman MC, Strauss BE. The DU145 human prostate carcinoma cell line harbors a temperature-sensitive allele of p53. Prostate 2006; 66:1455–62. [PubMed: 16741917]
45. Carroll AG, Voeller HJ, Sugars L, Gelmann EP. p53 oncogene mutations in three human prostate cancer cell lines. Prostate 1993; 23:123–34. [PubMed: 8104329]
46. Bensaad K, Tsuruta A, Selak MA, Vidal MN, Nakano K, Bartrons R, et al. TIGAR, a p53-inducible regulator of glycolysis and apoptosis. Cell 2006;126:107–20. [PubMed: 16839880]
47. Doherty JR, Cleveland JL. Targeting lactate metabolism for cancer therapeutics. J Clin Invest 2013;123:3685–92. [PubMed: 23999443]
48. Le A, Cooper CR, Gouw AM, Dinavahi R, Maitra A, Deck LM, et al. Inhibition of lactate dehydrogenase A induces oxidative stress and inhibits tumor progression. Proc Natl Acad Sci U S A 2010;107:2037–42. [PubMed: 20133848]
49. Choi SY, Xue H, Wu R, Fazli L, Lin D, Collins CC, et al. The MCT4 gene: a novel, potential target for therapy of advanced prostate cancer. Clin Cancer Res 2016;22:2721–33. [PubMed: 26755530]
50. Eales KL, Hollinshead KE, Tennant DA. Hypoxia and metabolic adaptation of cancer cells. Oncogenesis 2016;5:e190. [PubMed: 26807645]

Translational Relevance

Tumor reliance on glycolysis for energy production is considered a hallmark of cancer and correlates with tumor aggressiveness, poor prognosis, and advanced stage of disease in prostate cancer. Metabolic inhibitors are being developed as therapeutics, but sensitivity to these agents is challenging to predict. Noninvasive imaging strategies may provide a method to assess the metabolic state of tumors and predict sensitivity to targeting the Warburg effect. Hyperpolarized MRSI provides an opportunity to noninvasively interrogate the flux through an enzymatic reaction and allows for serial evaluation, potentially reflecting the real-time flux and tumor reliance on the imaged reaction. Hyperpolarized [1-^{13}C]-pyruvate MRSI has been performed in prostate cancer patients and evaluated as a biomarker for prostate cancer aggressiveness.

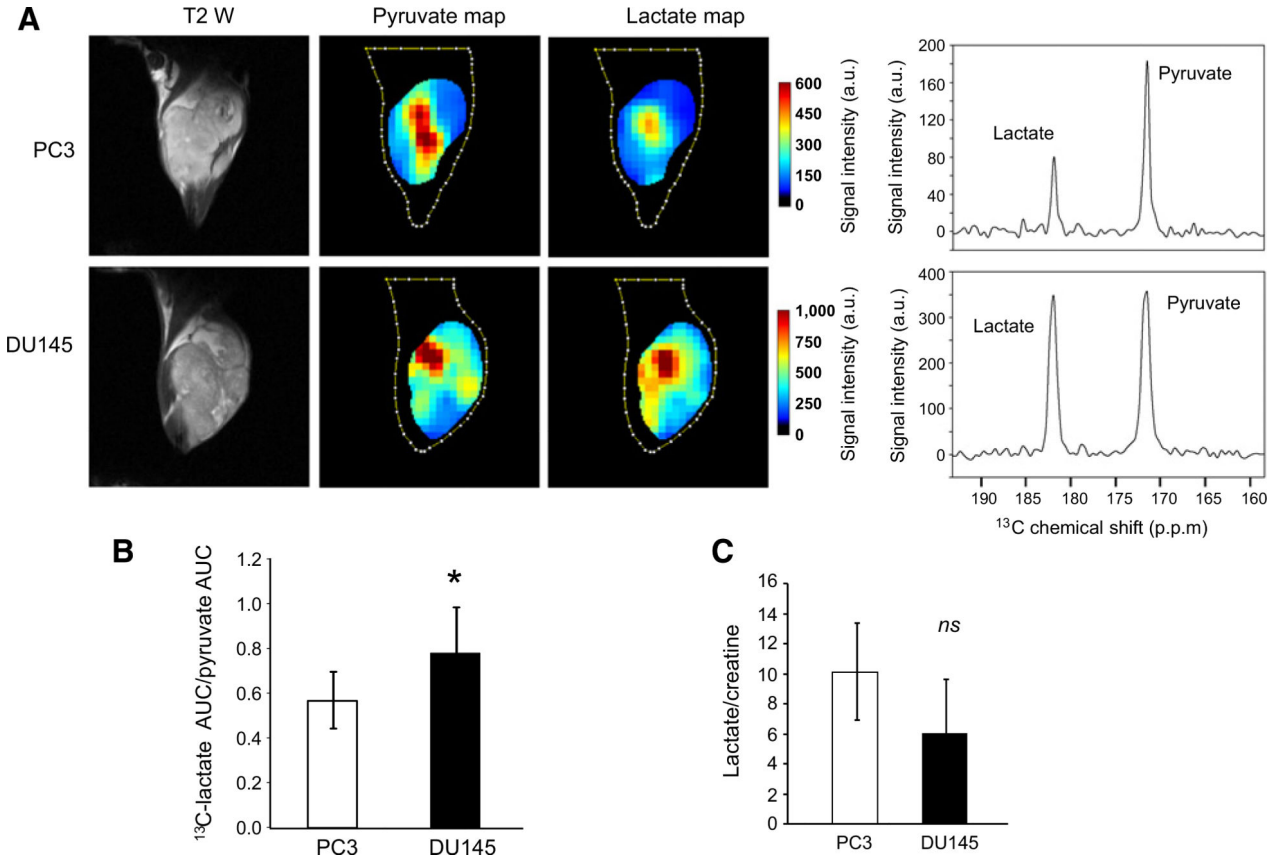

Figure 1.

Imaging lactate production in prostate cancer xenografts. PC3 and DU145 xenografts were grown in the hind leg of male athymic nu/nu mice. **A,** Axial T2-weighted images of representative xenografts with coordinating hyperpolarized ^{13}C pyruvate and ^{13}C lactate maps and corresponding spectra following the injection of hyperpolarized [1-^{13}C] pyruvate. Lactate and pyruvate maps and spectra represent average time intensity between 12 and 90 seconds after the start of the scan (injection of hyperpolarized [1-^{13}C] pyruvate at 10 seconds) in a representative tumor. The spectra demonstrate elevated levels of lactate in DU145 tumors compared with PC3 tumors. **B,** The ratio of the AUC of lactate to the AUC of pyruvate in DU145 and PC3 xenografts measured with hyperpolarized [1-^{13}C] pyruvate MRSI (n = 5 mice per cell line). **C,** The ratio of lactate to creatine in DU145 and PC3 xenografts as measured by ^{1}H-MRS. Bars, mean; error bars, SD; p.p.m., parts per million; *, $P < 0.05$ by paired t test; *ns*, not significant; $P \geq 0.05$ by paired t test.

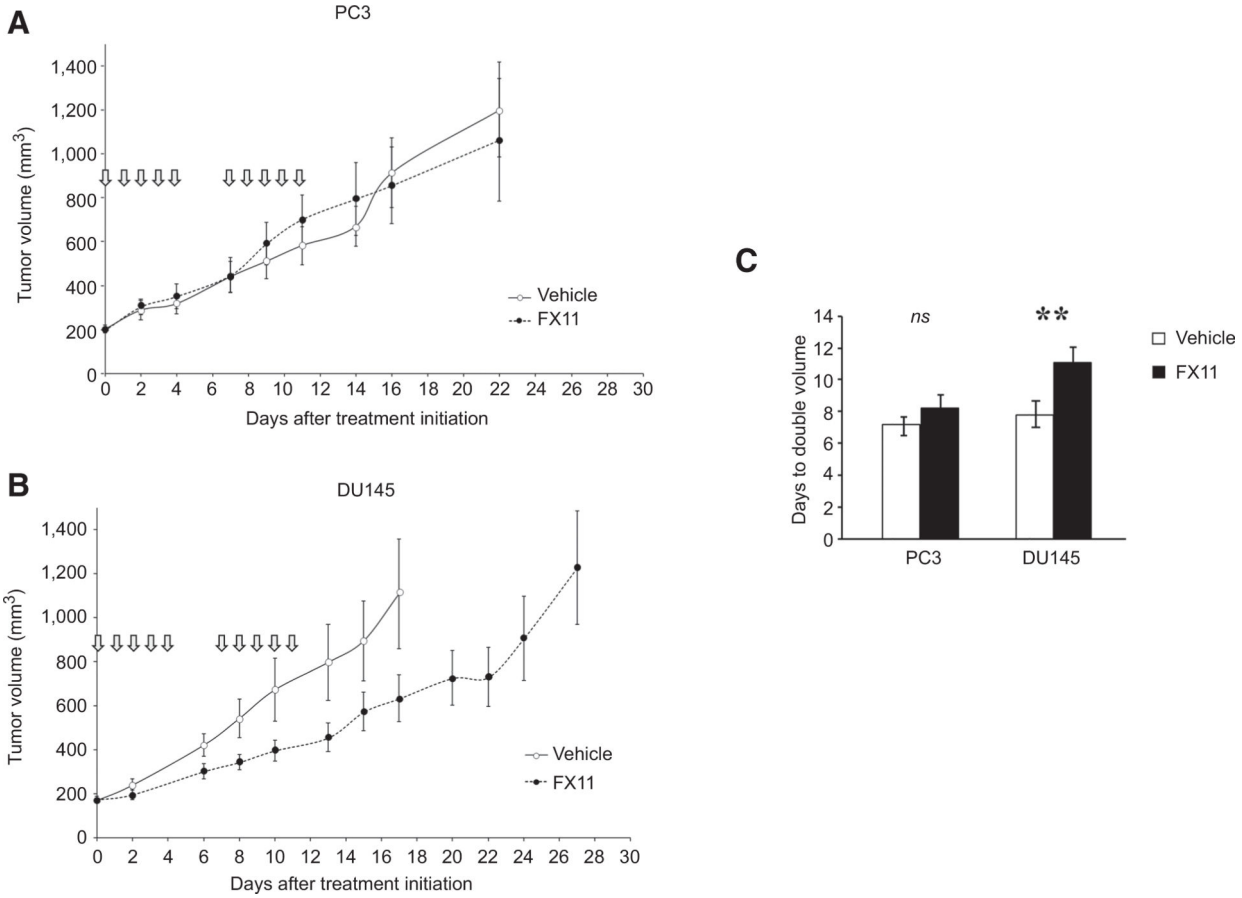

Figure 2.

Effects of LDHA inhibition in prostate cancer xenografts. DU145 and PC3 cells were injected subcutaneously into the right hind leg of male athymic nu/nu mice. Mice were randomized to treatment with vehicle or FX-11 (42 μg/mouse/day for 5 days × 2 weekly cycles). Tumors were followed until they reached 1,000 mm^3. The experiment was completed in triplicate. **A** and **B,** Representative growth curves. **C,** Tumor doubling time calculated from initiation of treatment including mice from triplicate experiments ($n = 24$ mice per treatment and condition). Bars, mean; error bars, standard error. *, $P < 0.05$ by ANOVA with Tukey correction; *ns*, not significant; $P \geq 0.05$ by ANOVA with Tukey correction.

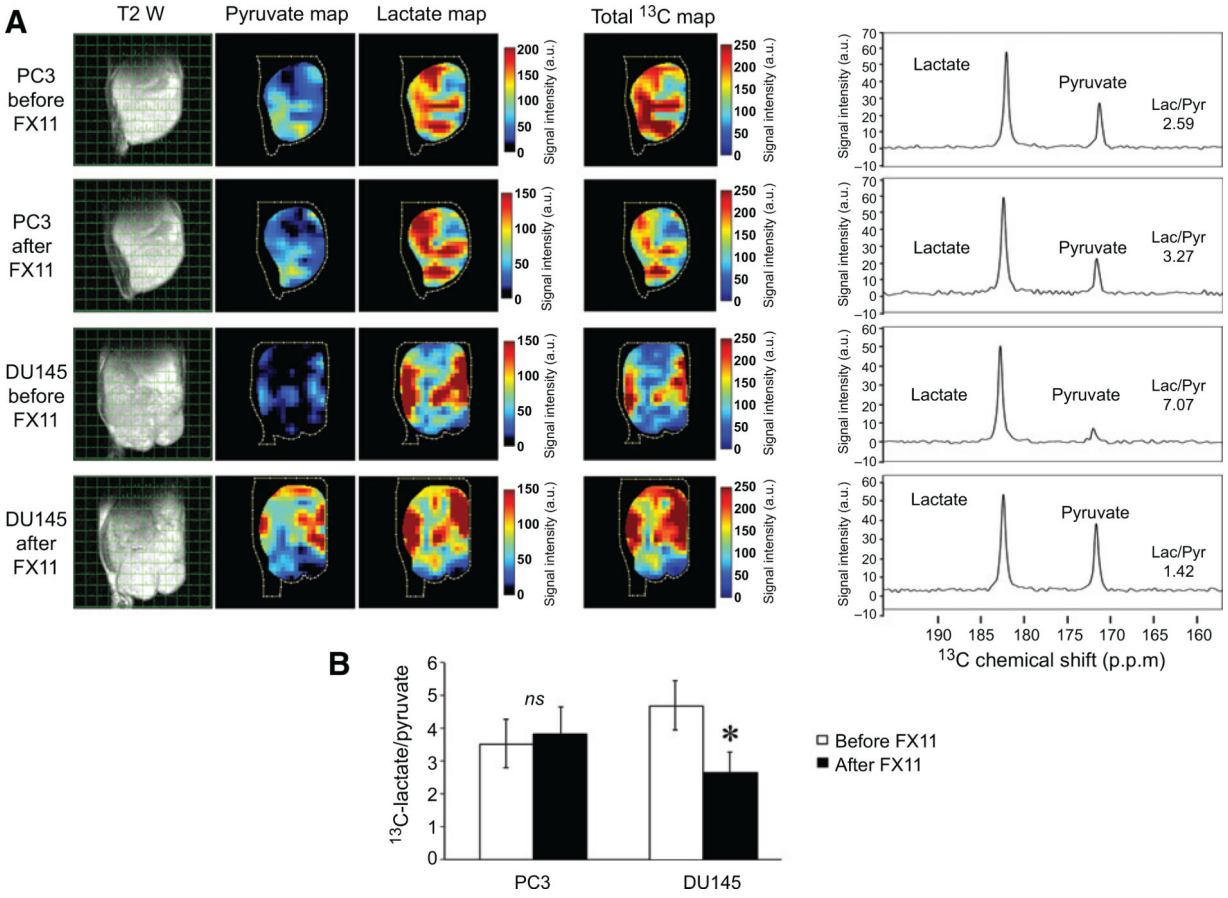

Figure 3.

Effects of FX-11 on lactate production in prostate cancer xenografts. PC3 and DU145 xenografts were grown in the hind leg of male athymic nu/nu mice. Established tumors were imaged with hyperpolarized [1-^{13}C] pyruvate MRSI immediately prior to the first treatment and 1 hour after the treatment with FX-11 (42 μg/mouse × 2 days). **A,** Axial T2-weighted image of PC3 and DU145 xenografts with coordinating hyperpolarized ^{13}C pyruvate and ^{13}C lactate maps and corresponding spectra following the injection of hyperpolarized [1-^{13}C] pyruvate before and after treatment with FX-11. The spectra demonstrate elevated levels of lactate in the DU145 tumors compared with the PC3 tumors. DU145 tumors exhibited a substantial change in pyruvate conversion to lactate after FX-11 treatment that was not observed in PC3 tumors. **B,** The ratio of hyperpolarized ^{13}C lactate to ^{13}C pyruvate in DU145 and PC3 xenografts measured with hyperpolarized [1-^{13}C] pyruvate MRSI ($n = 5$ mice per cell line and time point). Bars, mean; *, $P < 0.05$ by ANOVA with Tukey correction; *ns*, not significant; $P \geq 0.05$ by ANOVA with Tukey correction.

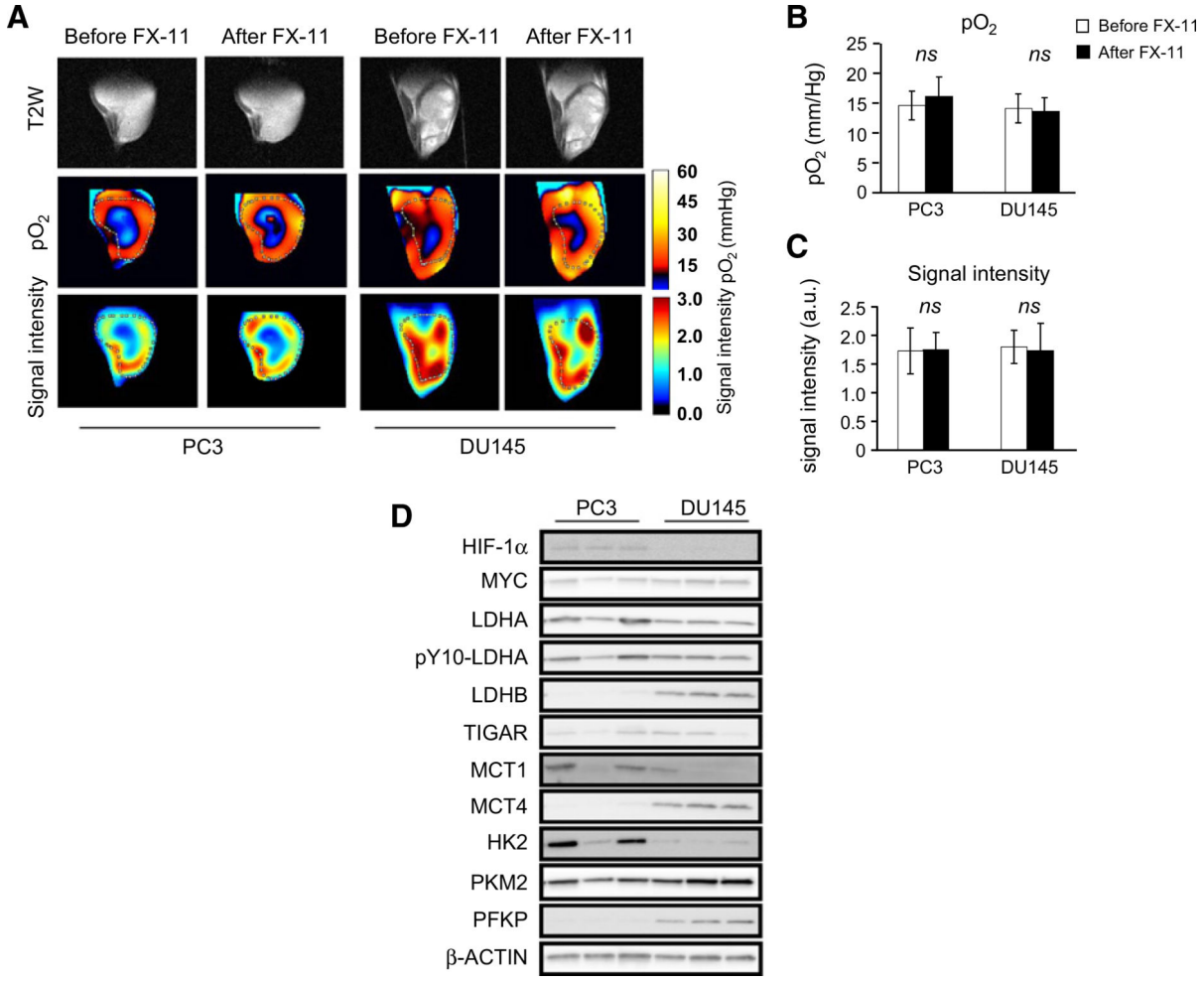

Figure 4.

Oxygenation and perfusion of DU145 and PC3 xenografts. PC3 and DU145 xenografts were grown in the hind leg of male athymic nu/nu mice. At approximately 1,000 mm^3 volume, tumors were imaged with EPR imaging 3 to 15 minutes after intravenous delivery of OXO63. **A,** Representative T2 anatomic images of DU145 and PC3 xenografts with coregistered EPR imaging (signal intensity and pO_2) before and after FX-11. Oxygenation within DU145 and PC3 xenografts as assessed by EPR imaging before and after FX-11 treatment. Perfusion was assessed by determining the signal intensity within imaged tumors. **B,** Median oxygenation within DU145 and PC3 xenografts as assessed by EPR imaging before and after FX-11 treatment ($n = 5$ mice per cell line and time point). **C,** Median signal intensity in DU145 and PC3 tumors before and after treatment with FX-11 (42 μg/mouse × 2 days). **D,** PC3 and DU145 xenografts were grown in the hind leg of male athymic nu/nu mice. At approximately 1,000 mm^3 volume, untreated tumors were harvested and probed with Western blot analysis of the indicated proteins using β-actin as the loading control. Bars, mean; error bars, SD. *ns*, not significant; $P \geq 0.05$ by ANOVA with Tukey correction.

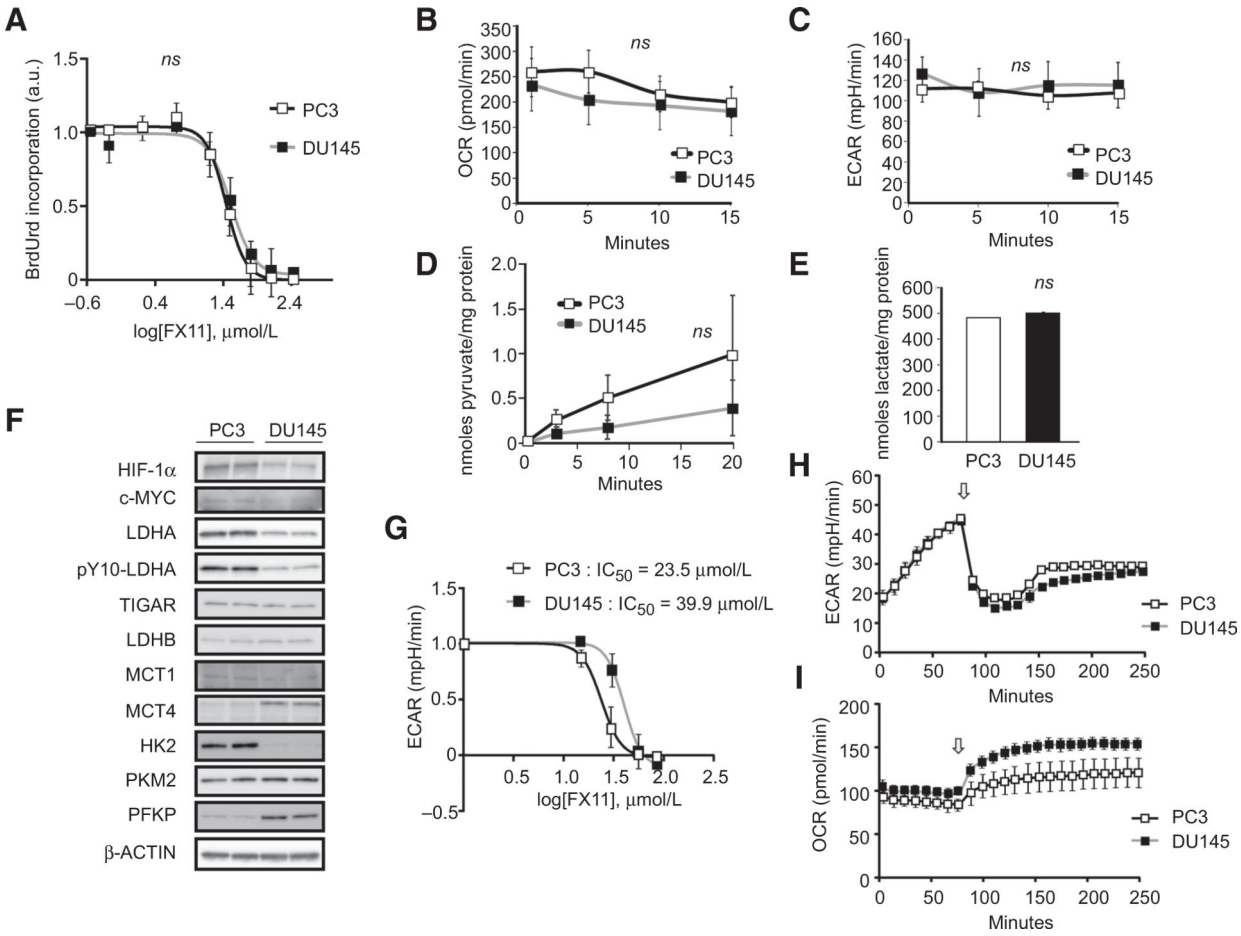

Figure 5.

In vitro analysis of the glycolytic state of DU145 and PC3 cell lines. Exponentially growing DU145 and PC3 tumor cells were utilized. **A,** Cells were exposed to varying concentrations of FX-11, and BrdU uptake was analyzed at 24 hours. **B** and **C,** Plated cells were incubated with XF assay medium, and OCR and ECAR were measured. **D,** Uptake of [2-^{14}C] pyruvic acid in DU145 and PC3 cells over 20 minutes was determined by assessing cell lysates using a scintillation counter and normalized to protein concentrations. **E,** Lactate content of exponentially growing tumor cells was measured and normalized to total protein. **F,** Exponentially growing untreated DU145 and PC3 cells were collected. The expression of the indicated proteins was determined with Western blotting of cell lysates using β-actin as the loading control. **G,** Cells were exposed to varying concentrations of FX-11, and ECAR was assessed at 140 minutes after FX-11 treatment. **H** and **I,** Plated cells were incubated with XF assay medium and treated at the indicated time point (arrow) with pyruvate (8.35 mmol/L) and OCR and ECAR were measured. Bars and points, mean; error bars, SD; *ns*, not significant; $P \geq 0.05$ by paired *t* test.

Table 1.

Steady-state metabolomic profiling of PC3 and DU145 tumors

	PC3[a]	DU145[a]	Ratio of the means (PC3:DU145)	*P*
Glucose-6-phosphate	27 ± 14	139 ± 73	0.2	0.113
Fructose-6-phosphate	9.3 ± 4.5	42 ± 21	0.2	0.103
Fructose-1,6-diphosphate	89 ± 28	100 ± 56	0.9	0.798
Dihydroxyacetone phosphate	35 ± 11	67 ± 47	0.5	0.365
Glyceraldehyde 3-phosphate	1.2 ± NA	3.2 ± 3	0.4	NA
3-phosphoglyceric acid	1.3 ± 0.4	2.8 ± 1.7	0.5	0.027
2-phosphoglyceric acid	0.2 ± NA	0.3 ± NA	0.06	NA
Phosphoenolpyruvic acid	ND	ND	ND	ND
Pyruvic acid	68 ± 19	113 ± 52	0.6	0.275
Lactic acid	11,597 ± 2,608	9,961 ± 1,268	1.2	0.403
Creatine	2,794 ± 735	4,549 ± 2,527	0.6	0.353
Lactic acid/pyruvic acid	173 ± 21	97 ± 27	1.8	0.021
Lactic acid/creatine	4.38 ± 1.7	2.56 ± 1.0	1.8	0.203
NAD^+	155 ± 30	232 ± 34	0.7	0.043
NADH	7.1 ± 0.08	5.7 ± 1.0	1.2	0.147
$NADH/NAD^+$	0.05 ± 0.01	0.02 ± 0.001	1.7	0.057

Abbreviations: NA, metabolite only detected in one tumor; ND, metabolite was not detected.

[a] nmol/gram of tumor, mean ± SD.